Polymer Journal
https://doi.org/10.1038/s41428-026-01205-1

ORIGINAL ARTICLE

Synthesis of poly(acetoacetoxyethyl methacrylate-*b*-dimethylsiloxane-*b*-acetoacetoxyethyl methacrylate) triblock copolymers *via* SARA ATRP for reaction-mediated microphase separation of sustainable vitrimers

Yi-Shen Huang[1,2] · Shibiru Yadeta Ejeta[1,3] · Shiao-Wei Kuo[4] · Yeo-Wan Chiang[4] · Yasuyuki Nakamura[2] · Chih-Feng Huang[1,5]

Received: 15 February 2026 / Revised: 2 May 2026 / Accepted: 6 May 2026

Abstract

Vitrimers offer a sustainable route to covalently crosslinked polymer networks with processability enabled by thermally activated bond-exchange reactions. However, the integration of programmable nanostructures into vitrimer networks remains challenging because of the competition between phase behavior and the curing process. Here, we report an environmentally conscious synthesis of ABA-type triblock copolymers (tBCPs), poly(acetoacetoxyethyl methacrylate-*b*-dimethylsiloxane-*b*-acetoacetoxyethyl methacrylate) (P(AAEMA-*b*-DMS-*b*-AAEMA)), using a supplemental activator and reducing agent (SARA) atom transfer radical polymerization (ATRP) technique. In this approach, a Br–poly(dimethylsiloxane)–Br (Br–PDMS–Br) macroinitiator and a low-concentration (ppm-level) $CuBr_2$ catalyst were used. The resulting high-χ tBCPs exhibited facile composition-dependent bulk morphologies spanning spheres, cylinders, and lamellae on a scale of approximately 30 nm, as confirmed by small-angle X-ray scattering (SAXS). Subsequently, vinylogous urethane vitrimer networks were prepared by crosslinking the β-ketoester (β-KE) units with hexamethylenediamine (HMDA) at 80 °C, followed by postcuring *via* hot-pressing at 160 °C. Compared with the tBCP precursor, vitrimerization markedly enhances the thermal resistance, thereby increasing the 5% weight-loss temperature ($T_{d,5\%}$) by 51 °C. The results of SAXS analysis before and after vitrimer formation revealed that curing/processing largely suppresses higher-order reflections and yields broadened primary maxima, indicating the formation of less long-range order and primarily nonordered microphase-separated structures. Mediating the NH_2/β-KE ratio (1 vs. 2) induces modest but systematic changes in the peak position and width, suggesting that the crosslink density affects segregation/coherence, while the reaction-mediated microphase separation (REMPS) pathway during curing governs primarily the loss of tBCP-derived lattice order. This study presents a scalable ATRP-to-vitrimer strategy for preparing PDMS-containing nanostructured networks and provides mechanistic insight into morphology evolution during vitrimerization.

Introduction

The development of polymer networks that combine the mechanical robustness of thermosets with processability and recyclability has become a central goal in the field of polymer science. In particular, vitrimers—containing covalently crosslinked networks that can topologically rearrange through thermally activated bond-exchange reactions—have emerged as a promising platform to bridge the long-standing gap between permanent thermosets and melt-processable thermoplastics [1–9]. Vitrimers provide a material concept that is attractive for sustainable manufacturing and circular use scenarios because they facilitate

Supplementary information The online version contains supplementary material available at https://doi.org/10.1038/s41428-026-01205-1.

✉ Yasuyuki Nakamura
NAKAMURA.Yasuyuki@nims.go.jp

✉ Chih-Feng Huang
HuangCF@dragon.nchu.edu.tw

Extended author information available on the last page of the article

Published online: 08 June 2026

stress relaxation and reshaping under appropriate thermal stimuli while retaining insolubility and dimensional stability at service temperatures. Despite this progress, translating vitrimer chemistry into materials with programmable nanostructures remains challenging because dynamic covalent bond (DCB) exchange, processing history, and phase behavior often compete in determining the final morphology and properties [10–12].

Diblock and triblock copolymers (dBCPs and tBCPs, respectively) offer an effective and well-established route to generate periodic nanostructures through microphase separation, in which the domain geometry (spheres, cylinders, lamellae, etc.) and characteristic length scales can be tailored by composition, segregation strength, and processing conditions [13–15]. When such self-assembled nanostructures are integrated into polymer networks, they may provide hierarchical architectures that simultaneously deliver mechanical reinforcement, transport control, and functional compartmentalization [16]. However, the incorporation of BCP-derived order into covalently adaptable networks is nontrivial. Notably, network formation can kinetically trap nonequilibrium morphologies. Conversely, bond exchange during annealing or processing can totally disrupt the long-range order. Therefore, the practical realization of nanostructured vitrimers requires a synthetic strategy that (i) produces well-defined BCP precursors with controlled molecular weights (MWs) and narrow dispersity, (ii) enables systematic variation in block volume fractions, and (iii) provides network formation under conditions compatible with preserving or predictably transforming nanostructures. Reversible-deactivation radical polymerization (RDRP) [17–21] techniques are highly effective for synthesizing reactive, well-defined BCPs with a controlled architecture and narrow polydispersity (PDI or $Đ$). Atom transfer radical polymerization (ATRP) [20], a representative RDRP technique, is significantly more convenient than other techniques, such as conventional radical polymerization, primarily because of its living nature and control. A major benefit of ATRP is its ability to easily attach various initiating groups (e.g., halogen esters) to polymer chain ends to create macroinitiators (MIs), thereby facilitating the synthesis of linear and branched BCPs. ATRP is also well known for its industrial adoption potential. Unlike other challenging synthesis approaches, RDRP techniques offer the benefit of polymerization transformation ($\mathcal{T}$) [22] and combination ($\mathcal{C}$) [23], facilitating the synthesis of specific copolymers using dissimilar chemistries. However, conventional ATRP relies on a relatively high catalyst loading (thousands of ppm) [24], which raises environmental concerns and complicates the purification process. To address these issues, environmentally conscious approaches have been developed, such as the supplemental activator and reducing agent (SARA) [25, 26], activators regenerated by electron transfer (ARGET) [27], and initiators for continuous activator regeneration (ICAR) [28]. ATRP techniques. In these methods, the concentration of transition metal catalysts is significantly reduced, often to only tens to hundreds of ppm [29]. Furthermore, these approaches exhibit increased oxygen tolerance [30, 31], making the process easier, more cost-effective, environmentally friendly, and broadly applicable without sacrificing MW or dispersity control.

In addition, reaction-induced microphase separation (RIMPS) [18, 32], and the closely related concept of polymerization-induced microphase separation (PIMS) [33], not only provides an efficient route to directly generate micro- to nanoscale morphologies but also targets high-performance polymer matrices. When BCPs comprising mutually incompatible blocks are employed, the developing thermodynamic driving force during curing/polymerization can induce in situ phase separation, yielding well-defined microstructures through RIMPS/PIMS and/or self-assembly pathways [34]. In our previous study, for example, we reported the addition of PCL-*b*-PnBA BCPs to photoresists to fabricate transparent, temperature-resistant nanostructured polymer materials through microphase separation during photocuring and enhanced the flexibility and adhesion with morphology development [35]. To differentiate the analogy, this process can be denoted reaction-mediated microphase separation (REMPS), which essentially involves self-assembly pathways throughout the (photo)curing procedures. In summary, RIMPS/PIMS/REMPS can reduce the number of processing steps while enabling morphology control, increasing mechanical stability, and enhancing pattern fidelity [36]. The broad compatibility with diverse material platforms and the potential for solvent-free or aqueous processing further position RIMPS/PIMS/REMPS as attractive strategies for developing environmentally friendly and multifunctional polymer systems [36, 37]. Unlike previously reported BCP vitrimers [38–40], in addition, we employ an environmentally conscious SARA ATRP technique with only ppm-level catalysts to synthesize well-defined ABA-type tBCPs. By incorporating a flexible poly(-dimethylsiloxane) (PDMS) midblock with a low solubility parameter, this method produces poly(acetoacetoxyethyl methacrylate-*b*-dimethylsiloxane-*b*-acetoacetoxyethyl methacrylate) (P(AAEMA-*b*-DMS-*b*-AAEMA)) precursors that exhibit a high interaction parameter (high-χ).

As shown in Scheme 1a, we employed an environmentally conscious ATRP approach (specifically, SARA ATRP) for synthesizing well-defined ABA-type triblock copolymers. We extended the chain of the Br–PDMS–Br macroinitiator to obtain P(AAEMA-*b*-DMS-*b*-AAEMA), thereby using significantly reduced amounts of catalyst for precise polymer synthesis. As shown in Scheme 1b, vinylogous urethane vitrimers were first prepared from P(AAEMA-*b*-

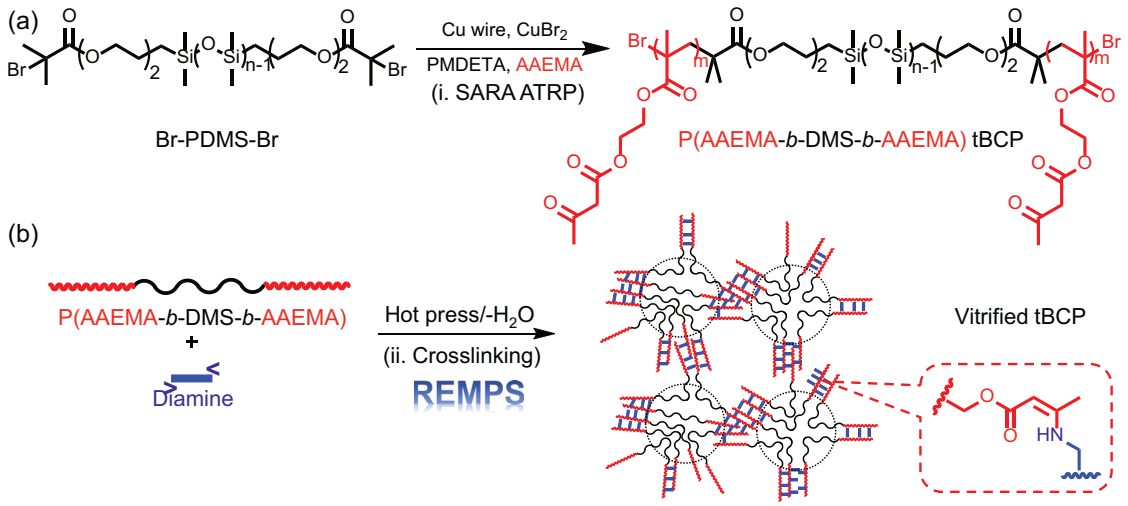

Scheme 1 **a** Chain extension of Br–PDMS–Br MI with AAEMA *via* SARA ATRP. **b** Crosslinking of the P(AAEMA-*b*-DMS-*b*-AAEMA) tBCP and diamine *via* the formation of vinylogous urethane moieties and REMPS of sustainable vitrimers

DMS-*b*-AAEMA) tBCPs using hexamethylenediamine (HMDA) as a crosslinker in various equivalent ratios of amine and β-ketoester to mediate REMPS. The thermal stability of the tBCPs and cured tBCPs was examined via thermogravimetric analysis (TGA). The morphologies of the pristine high-χ tBCPs and cured tBCPs in a bulk film state were characterized through small-angle X-ray scattering (SAXS).

Experimental

Materials

2-Bromoisobutyryl bromide (BiB, 97%), copper wire (Cu wire (diameter = 1.0 mm), 99.9%), copper dibromide ($CuBr_2$, 99%), hydrochloric acid (37%), anhydrous magnesium sulfate ($MgSO_4$, 99%), naphthalene (99%), *N*,*N*,*N*',*N*'',*N*''-pentamethyldiethylenetriamine (PMDETA, 98%), sodium chloride (NaCl, 99%), triethylamine (TEA, 99.5%), two commercial types of bis(hydroxyalkyl) terminated poly(dimethylsiloxane) (HO-PDMS-OH, with $M_{n,NMR}$ values of 8,460 and 10,520), anisole (99%), methanol (MeOH, 99%), HMDA (98%), tetrahydrofuran (THF, 99%), and naphthalene were purchased from Sigma–Aldrich and used without purification. Acetoacetoxyethyl methacrylate (AAEMA, 95%) was purchased from TCI and purified prior to use by passing it through a basic alumina column. Toluene (99%) was dried via distillation with sodium before use.

Characterization

Monomer conversion was monitored through gas chromatography (GC; Hewlett Packard 5890 Series II) equipped with a flame ionization detector (FID) and a CNW CD-5 capillary column (30 m), using naphthalene as an internal standard. Gel permeation chromatography (GPC) measurements were conducted at 40 °C with THF as the eluent (flow rate: 1.0 mL/min) on a system equipped with a Waters 515 pump, a Waters 410 differential refractometer, a Waters 486 ultraviolet–visible (UV–vis) absorbance detector, and two PSS SDV columns (linear S and 100 Å). The number-average molecular weight (M_n), weight-average molecular weight (M_w), and polydispersity (PDI = M_w/M_n) were determined on the basis of monodisperse poly(methyl methacrylate) (PMMA) standards for calibration. Proton nuclear magnetic resonance (^{1}H NMR) spectra were recorded on a Varian 400 MHz spectrometer using $CDCl_3$ as the solvent, with the residual solvent signal referenced at $\delta = 7.26$ ppm. TGA was conducted on a TA Instruments Q50 instrument under a nitrogen atmosphere using a platinum pan at a heating rate of 20 °C/min over the temperature range of 30–700 °C. SAXS experiments were conducted at the National Synchrotron Radiation Research Center (NSRRC, Hsinchu, Taiwan) beamline BL23A1. The sample-to-detector distance was set to 3.0 m, and the X-ray energy was set to 15 keV. Scattering patterns were collected with a Pilatus-1M-F detector and plotted as the scattering intensity (I) versus the scattering vector magnitude, $q = (4\pi/\lambda)\sin(\theta/2)$. The domain spacing (d) was calculated from the position of the primary scattering peak (q*) according to $d = 2\pi/q^*$.

Chain extension of Br–PDMS–Br with AAEMA through SARA ATRP

Br–PDMS–Br was synthesized through an acylation reaction [18]. AAEMA (4.5 mL, 20 mmol), Br–PDMS–Br (1 g,

0.1 mmol), $CuBr_2$ (1 mg, 0.04 mmol), naphthalene (0.2 g), THF (8 mL), and a stir bar with fresh copper wire (5 mm) were added to a sealed Schlenk flask. Deoxygenation was conducted over three freeze–pump–thaw cycles. Then, PMDETA (60 µL, 0.3 mmol) was injected into the flask with a microsyringe, and polymerization was achieved at 60 °C. Samples were collected periodically under a nitrogen blanket and passed through a short column of neutral alumina to remove dissolved copper salts before GC and GPC analyses. The initiation efficiency ($I_{eff} = M_{n,th(PAAEMA)}/M_{n,NMR(PAAEMA)}$) was estimated on the basis of the PAAEMA segment via NMR analysis [41]. The reaction mixture was quenched to room temperature and diluted with THF. The solution was passed through a neutral alumina column to remove residual copper complex and precipitated in MeOH. The collected polymer was vacuum-dried to obtain PAAEMA-*b*-PDMS-*b*-PAAEMA tBCP ($M_{n,NMR} = 14{,}930$, $M_{n,GPC} = 21{,}580$, PDI = 1.48, and yield = 32%).

Preparation of vinylogous urethane vitrimers and reprocessing

Vinylogous urethane vitrimers were prepared from PAAEMA-*b*-PDMS-*b*-PAAEMA tBCPs using HMDA as the crosslinker. Notably, the tBCP was first dissolved in THF to obtain a homogeneous solution. HMDA was then added in a stoichiometric amount relative to the β-ketoester (AAEMA) functionalities (0.5 equivalent mole of HMDA per AAEMA unit, which is based on two amine groups per HMDA molecule), and the mixture was stirred until complete homogenization was achieved. The resulting solution was cast into a mold, and the solvent was allowed to evaporate, followed by curing at 80 °C to yield crosslinked films *via* the sufficient formation of vinylogous urethane linkages. During the postcuring process, the films were subsequently hot-pressed at 160 °C under 3 bars to obtain bulk vitrimer specimens. For practical use, this hot-pressing step serves as a dynamic annealing process that drives morphological transformations. With respect to the reprocessing procedures, similarly, two steps were conducted, namely, reprocessing at 80 °C for 0.5 h and 160 °C for 2 h under 6 bars.

Results and discussion

In SARA ATRP chain extension of Br–PDMS–Br with AAEMA, the polymerization kinetics and evolution of the MW notably depended on the $CuBr_2$ loading (Fig. 1). At 200 ppm, for $CuBr_2$ (AAEMA/Br–PDMS–Br/$CuBr_2$/PMDETA = 200/1/0.04/0.3 at 60 °C; Cu wire 5 mm; $[AAEMA]_0$ = 1.6 M), curve a of the semilogarithmic kinetic plot in Fig. 1A was initially linear, yielding an apparent rate constant of $k_{app} \approx 5.10 \times 10^{-5}$ s^{-1}. After approximately 3 h, the polymerization indicated a slight deviation from the ideal first-order kinetics. The corresponding MW analysis results (triangles in Fig. 1B, C) also revealed only a slight increase in the PDI and a high initiation efficiency ($I_{eff} = M_{n,th(PAAEMA)}/M_{n,NMR(PAAEMA)} \approx$ 91%). Importantly, the GPC traces (Fig. 2A) exhibited a gradual shift toward higher MWs while maintaining a monomodal distribution, supporting the occurrence of continuous chain extension. These results suggest that although a minor deviation between the theoretical and experimental MWs was observed under these conditions, the polymerization still proceeded in a controlled manner with effective chain growth. When the concentration of the $CuBr_2$ catalyst was increased to 250 ppm to improve control (AAEMA/Br–PDMS–Br/$CuBr_2$/PMDETA = 150/1/0.075/0.3 at 60 °C; Cu wire 5 mm), a linear first-order kinetic regime over an extended time window (up to ~7 h) was observed (curve b; Fig. 1A), with $k_{app} \approx 6.73 \times 10^{-5}$ s^{-1}. In parallel, the data in Fig. 1B, C (diamonds) revealed that the PDI remained low (<1.50) and M_n increased nearly linearly with conversion. The GPC traces (Fig. 2B) shifted progressively to higher MWs while retaining a monomodal distribution, supporting the occurrence of a controlled chain extension process with a high I_{eff} value (89%). At 500 ppm,

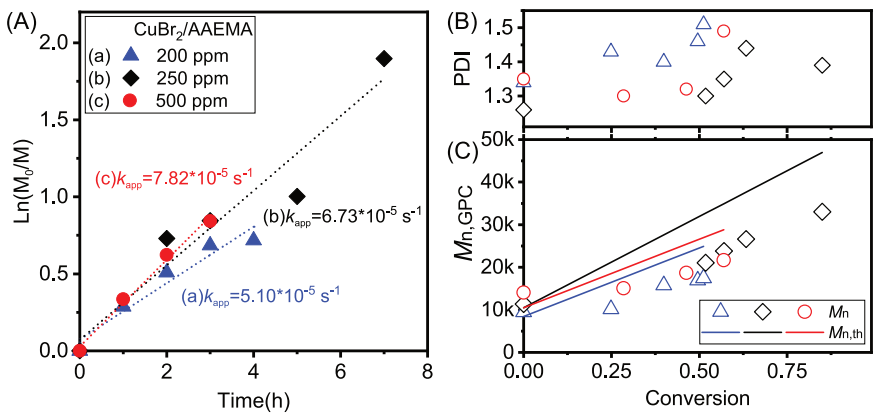

Fig. 1 Chain extension kinetics of Br–PDMS–Br MI with AAEMA at different ratios of $CuBr_2$/AAEMA (in ppm). **A** Ln vs. t, **B, C** PDI and $M_{n,GPC}$ vs. conversion (AAEMA/Br–PDMS–Br/$CuBr_2$/PMDETA = 200 or 150/1/x/3 at 60 °C; $[AAEMA]_0 = 1.6$ M in THF; notes: M/MI = 200 for exp. a (blue triangles) and c (red circles) and M/MI = 150 for exp. b (black diamonds)

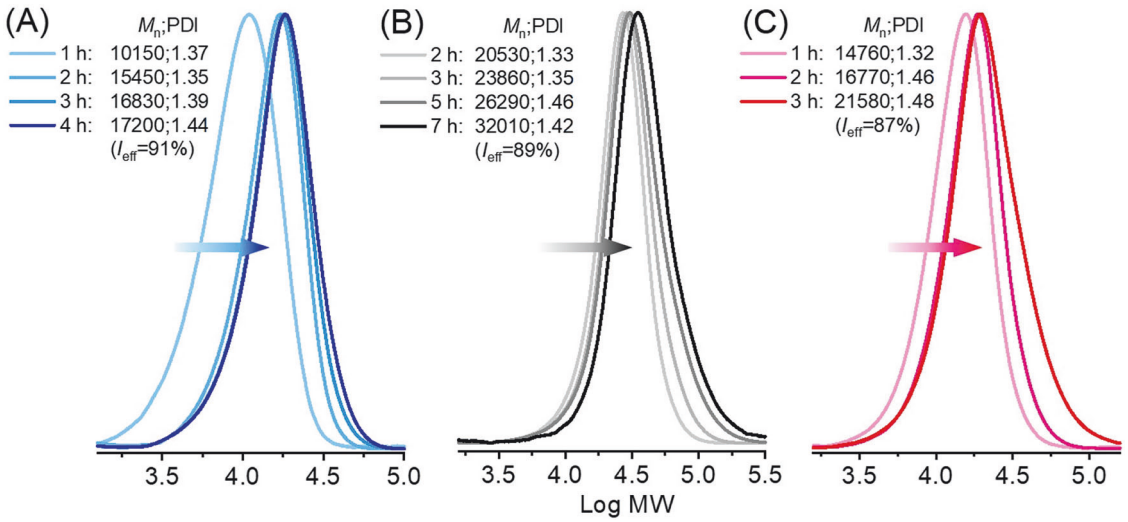

Fig. 2 Corresponding GPC traces for the chain extensions of Br–PDMS–Br MI with AAEMA *via* SARA ATRP with various amounts of $CuBr_2$. **A** 200 ppm, **B** 250 ppm, and **C** 500 ppm

for $CuBr_2$ (AAEMA/Br–PDMS–Br/$CuBr_2$/PMDETA = 200/1/0.05/0.3 at 60 °C; Cu wire 5 mm), the polymerization proceeded more rapidly, with the highest apparent rate ($k_{app} \approx 7.82\times10^{-5}$ s^{-1}), and the conversion rate reached comparable values within ~3 h (curve c, Fig. 1A). MW growth remained approximately linear with conversion with a low PDI (<1.50) (i.e., circles in Fig. 1B, C), and the corresponding GPC traces (Fig. 2C) revealed clear monomodal peak shifts. Under these optimized conditions, the obtained tBCP exhibited an acceptable I_{eff} value (87%), indicating a closer match between the theoretical and experimental MWs and more reliable chain-end initiation/propagation during extension. The results are summarized in Table 1.

The chemical structures and chain-end fidelity of the PDMS precursor, the brominated macroinitiator, and the resulting tBCP were examined via ^{1}H NMR spectroscopy (400 MHz, $CDCl_3$), and the results are shown in Fig. 3. With respect to HO–PDMS–OH (Fig. 3A), resonance assigned to the terminal methylene protons adjacent to the hydroxyl groups (peak a, ~3.7 ppm) was clearly observed, together with the characteristic PDMS backbone methyl signal (peak f, ~0.0 ppm). After esterification to form Br–PDMS–Br (Fig. 3B), the emergence of a new methylene signal next to the α-bromoisobutyrate ester signal (peak a′, ~4.3 ppm) and the corresponding α-bromoisobutyrate methyl signal (peak g, ~1.9 ppm) indicated successful chain-end functionalization. The high chain-end integrity of the macroinitiator was further supported by end-group analysis using the integral ratio of g (12*H*) to a′ (4*H*), from which the MW of Br–PDMS–Br was estimated as $M_{n,NMR} \approx 8460$ (corresponding to m ≈ 106 repeating units). Following SARA ATRP chain extension with AAEMA, the spectrum of P(AAEMA-*b*-DMS-*b*-AAEMA) (Fig. 3C) retained the resonance signal of PDMS methyl at ~0.0 ppm (i.e., the inner segment of the tBCP) while revealing additional signals characteristic of the PAAEMA outer blocks. In particular, the AAEMA side chain methylene protons (peak h set, ~4.25 ppm), β-dicarbonyl methylene (peak i, ~3.55 ppm), and acetoacetyl methyl group (peak j, ~2.3 ppm) were assigned, thus confirming the successful incorporation of AAEMA segments at both chain ends. Collectively, these spectral features can be applied to verify the formation of well-defined PAAEMA-*b*-PDMS-*b*-PAAEMA tBCPs (Table 2). In the subsequent discussion, PAAEMA-*b*-PDMS-*b*-PAAEMAs are abbreviated as $A_mD_nA_m$, where A_m denotes the PAAEMA segment with m repeating units, and D_n denotes the PDMS segment with n repeating units.

By pairing various polymer blocks, PDMS-based BCPs can provide an excellent system as high-χ BCPs because of

Table 1 Chain extensions of Br–PDMS–Br MI with AAEMA *via* SARA ATRP

Entry	$M_{n,NMR}$ of Br–PDMS–Br	Time (h)	$k_{app}\times10^5$ (s^{-1})	$M_{n,th}$	$M_{n,NMR}$	$I_{eff.}$ (%)[c]
1[a]	8460	4	5.10	16,460	18,100	91
2[b]	10,520	6	6.73	36,420	40,870	89
3[a]	10,520	3	7.82	12,200	14,100	87

[a]AAEMA/Br–PDMS–Br/$CuBr_2$/PMDETA = 200/1/0.1/x/0.3 with Cu wire (diameter =1 mm; length = 5 mm) ($[AAEMA]_0$ = 1.6 M in THF at 60 °C; x/AAEMA = 200 or 500 ppm)

[b]AAEMA/Br–PDMS–Br/$CuBr_2$/PMDETA = 150/1/0.075/0.3, Cu wire (diameter =1 mm; length = 5 mm) ($[AAEMA]_0$ = 1.6 M in THF at 60 °C)

[c]I_{eff} (initiation efficiency) = $M_{n,th(PAAEMA)}/M_{n,NMR(PAAEMA)}$

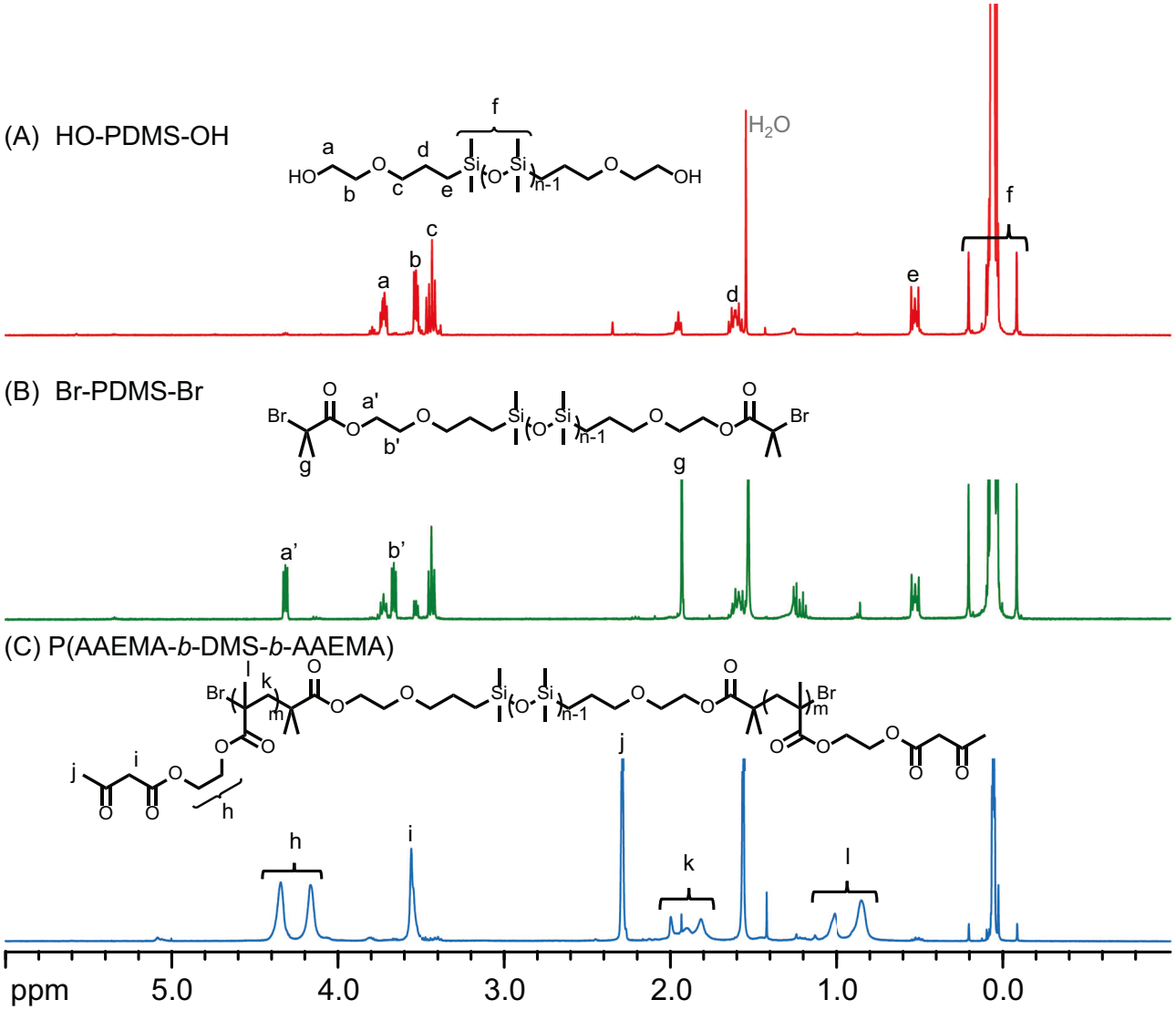

Fig. 3 ^{1}H NMR spectra (400 MHz, $CDCl_3$) of **A** HO-PDMS-OH, **B** Br–PDMS–Br, and **C** P(AAEMA-*b*-DMS-*b*-AAEMA) tBCP

Table 2 Characterization of the composition, volume fraction (Φ), and molecular weight of P(AAEMA-*b*-DMS-*b*-PAAEMA) tBCPs

Sample codes[a]	Compositions	Φ_{PDMS}	$M_{n,NMR}$	$M_{n,GPC}$	PDI
$A_{43}D_{61}A_{43}$	P($AAEMA_{43}$-*b*-DMS_{61}-*b*-$AAEMA_{43}$)	0.24	22,820	32,010	1.42
$A_{25}D_{69}A_{25}$	P($AAEMA_{25}$-*b*-DMS_{69}-*b*-$AAEMA_{25}$)	0.38	16,420	17,200	1.44
$A_{21}D_{82}A_{21}$	P($AAEMA_{21}$-*b*-DMS_{82}-*b*-$AAEMA_{21}$)	0.47	14,930	21,580	1.48

[a] $A_mD_nA_m$ denotes the samples in the later discussion, where A_m denotes the PAAEMA segment with m repeating units, and D_n denotes the PDMS segment with n repeating units

[b] The composition, volume fraction, and $M_{n,NMR}$ of tBCPs were estimated using $DP_{AAEMA(NMR)}$ ($M_{n,NMR} = M_{n,MI(NMR)} + MW_{AAEMA} \times DP_{AAEMA(NMR)}$; $\rho_{PDMS} = 0.965$ and $\rho_{PAAEMA} = 1.263$ g/cm^3)

their low solubility parameter ($\delta_{PDMS} = 15.1$ MPa). Thus, the bulk-state morphologies were subsequently examined. Bulk films of $A_{43}D_{61}A_{43}$, $A_{25}D_{69}A_{25}$, and $A_{21}D_{82}A_{21}$ were prepared via solution casting from 5 wt% THF, followed by evaporation at ambient temperature for 24 h. Subsequently, the films were thermally annealed at 160 °C under vacuum for 12 h to promote equilibration. The SAXS profiles of the thermally annealed tBCPs (Fig. 4A) revealed well-defined, composition-dependent microphase-separated morphologies. The profile of the low-PDMS composition sample $A_{43}D_{61}A_{43}$ (4 A(i): $\Phi_{PDMS} = 0.24$) exhibited peak positions consistent with spherical ordering (q/q* = 1:2:$\sqrt{12}$) with a domain spacing of d ≈ 29.2 nm. Increasing the volume fraction of PDMS to $A_{25}D_{69}A_{25}$ (4 A(ii): $\Phi_{PDMS} = 0.36$)

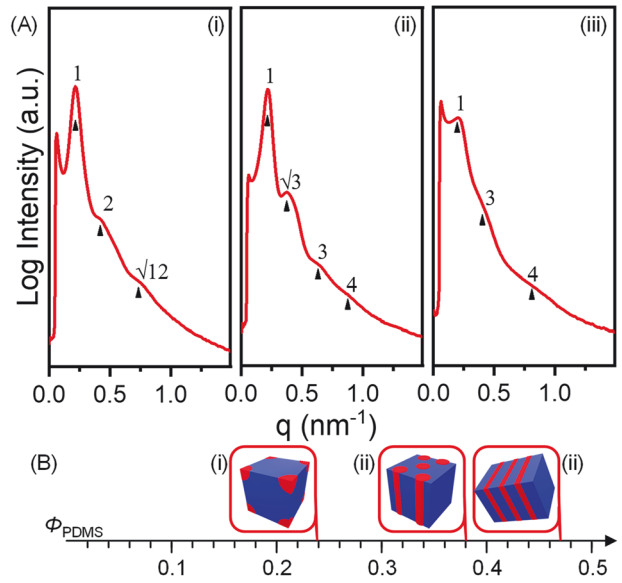

Fig. 4 A SAXS profiles of (i) $A_{43}D_{61}A_{43}$ ($\Phi_{PDMS} = 0.24$), (ii) $A_{25}D_{69}A_{25}$ ($\Phi_{PDMS} = 0.38$), and (iii) $A_{21}D_{82}A_{21}$ ($\Phi_{PDMS} = 0.47$) bulk films. **B** Relationship between the morphology and Φ_{PDMS}

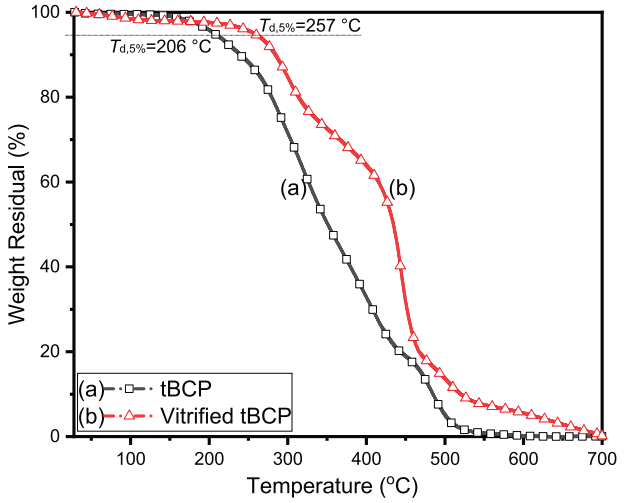

Fig. 5 TGA traces (ramping: 20 °C/min under $N_{2(g)}$) of **a** $A_{25}D_{69}A_{25}$ tBCP and **b** vitrimerized $A_{25}D_{69}A_{25}$ with HMDA via hot-pressing under 3 bars (80 °C for 0.5 h and 160 °C for 2 h)

resulted in a transition to cylindrical ordering, as indicated by the characteristic reflections (q/q* = 1:√3:3:4) and a comparable periodicity (d ≈ 28.9 nm). For the highest-PDMS composition $A_{21}D_{82}A_{21}$ (4 A(iii): $\Phi_{PDMS} = 0.47$), the SAXS pattern was consistent with a lamellar-type morphology (q/q* = 1:3:4) with d ≈ 31.4 nm. The relationship between the morphology and Φ_{PDMS} is shown in Fig. 4B. These results confirm that such a high-χ tBCP can easily enable access to spherical/cylindrical/lamellar morphologies across a moderate composition range, thereby providing a robust baseline for evaluating structural changes.

Afterward, we prepared vinylogous urethane vitrimers with HMDA as the crosslinker *via* curing at 80 °C and hot-pressing at 160 °C under 3 bars for 2 h. TGA was employed to compare the thermal stability between an example of $A_{25}D_{69}A_{25}$ tBCP and its HMDA-crosslinked vinylogous urethane vitrimer (Fig. 5). Compared with the linear precursor sample, the vitrimerized sample exhibited a systematic delay in mass loss across the entire main degradation window. Notably, vitrimerization led to a pronounced increase in the initial thermal resistance, as indicated by the 5% weight-loss temperature ($T_{d,5\%}$), which shifted from 206 °C (curve a) for the pristine tBCP to 257 °C (curve b) after crosslinking ($\Delta T_{d,5\%} = +51$ °C). The degradation in the vitrimerized material comprised a broader and more stepwise process, revealing an extended intermediate plateau before the steep mass decrease, whereas the pristine tBCP exhibited a more continuous decay. This behavior is consistent with network formation, which introduces additional thermally stable linkages and restricts segmental mobility, thereby facilitating the redistribution of degradation events over a wider temperature range. Collectively, these quantitative trends confirm that converting $A_{25}D_{69}A_{25}$ tBCP into a vinylogous urethane vitrimer *via* HMDA increases thermal robustness and resistance during pyrolysis. The pristine crosslinked $A_{25}D_{69}A_{25}$ tBCP, as shown in Fig. S1a (Supplementary Material), was immersed in THF for 24 h to evaluate its chemical stability. As shown in Fig. S1b, c the bulk film exhibited suitable solvent resistance and maintained its structural integrity. Furthermore, the inherent flexibility of the vitrimerized $A_{25}D_{69}A_{25}$ network, attributed to the incorporation of low-T_g PDMS segments, is shown in Fig. S2. Material reprocessability was confirmed through successful fragmentation and subsequent recovery, as shown in Fig. S3. These results collectively verify the successful preparation of P(AAEMA-*b*-DMS-*b*-AAEMA)-based vitrimers.

For practical considerations, the hot-pressing step functions as a dynamic annealing process. Therefore, we investigated the morphological evolution of the tBCPs following their conversion into vinylogous urethane vitrimers (Fig. 6). Vitrimer films were prepared by mixing $A_{43}D_{61}A_{43}$ (Fig. 6A), $A_{25}D_{69}A_{25}$ (Fig. 6B), and $A_{21}D_{82}A_{21}$ (Fig. 6C) with HMDA at prescribed NH_2/β-ketoester (β-KE) ratios (NH_2/β-KE = 1 and 2), followed by curing at 80 °C for 0.5 h and compression molding at 160 °C for 2 h. The pristine tBCPs (black curves) exhibited a composition-dependent ordered morphology. In contrast, after vitrimer formation (blue and red curves), the higher-order reflections were largely suppressed for all compositions, and the SAXS profiles were dominated by broadened primary maxima, indicating a pronounced reduction in long-range lattice

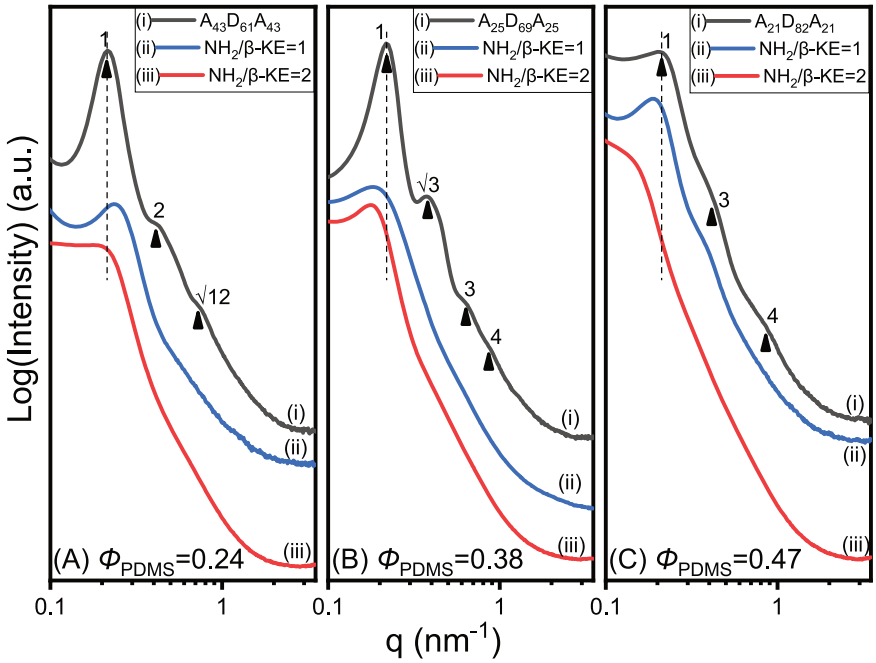

Fig. 6 SAXS profiles of (i) tBCPs and HMDA-cured tBCPs with (ii) NH_2/β-KE = 1 and (iii) NH_2/β-KE = 2 [equivalent molarities of amine (NH_2) and β-ketoester (β-KE) are from the HMDA compound and PAAEMA segment, respectively]. **(A)** $A_{43}D_{61}A_{43}$ series, **(B)** $A_{25}D_{69}A_{25}$ series, and **(C)** $A_{21}D_{82}A_{21}$ series

Table 3 Characteristics of the morphology of tBCP and cured tBCP bulk films obtained via SAXS

Sample	Φ_{PDMS}[a]	SAXS results	
		Morphology[b]	d (nm)
Pristine tBCPs			
$A_{43}D_{61}A_{43}$	0.24	SPH	29.2
$A_{25}D_{69}A_{25}$	0.38	CYL	28.9
$A_{21}D_{82}A_{21}$	0.47	LAM	31.4
tBCP with NH_2/β-KE = 1			
cured $A_{43}D_{61}A_{43}$	0.19	SPH	26.4
cured $A_{25}D_{69}A_{25}$	0.31	SPH	33.9
cured $A_{21}D_{82}A_{21}$	0.36	LAM	32.7
tBCP with NH_2/β-KE = 2			
cured $A_{43}D_{61}A_{43}$	0.15	Non SPH	30.4
cured $A_{25}D_{69}A_{25}$	0.26	SPH	35.4
cured $A_{21}D_{82}A_{21}$	0.31	Non SPH	–

[a]Φ_{PDMS}: volume fraction of the PDMS segment ($\rho_{PDMS} = 0.965$, $\rho_{HMDA} = 0.84$, and $\rho_{PAAEMA} = 1.263$ g/cm^3)

coherence and the emergence of predominantly nonordered microphase-separated structures. The profiles of the vitrimerized $A_{43}D_{61}A_{43}$ samples revealed primary peaks at q* = 0.237 and 0.215 nm for NH_2/β-KE = 1 and 2, respectively, corresponding to d = 26.4 and 30.4 nm, respectively. With respect to $A_{25}D_{69}A_{25}$ after vitrimerization, the primary maxima shifted to lower q values (q* = 0.185 and 0.177 nm^{-1}, respectively), resulting in larger characteristic spacings of d = 33.9 and 35.4 nm for NH_2/β-KE = 1 and 2, respectively, which is consistent with the coarsened, nonordered spherical-like segregation observed after network formation. In the case of $A_{21}D_{82}A_{21}$, the NH_2/β-KE = 1 vitrimer profile exhibited a primary peak at q* = 0.192 nm^{-1} (d = 32.7 nm), whereas the NH_2/β-KE = 2 profile was substantially broadened such that q* could not be reliably assigned, supporting the loss of well-defined long-range order upon vitrimerization. Varying the stoichiometry from NH_2/β-KE = 1 to 2 modestly modulates the peak position and width in the profile of each composition, suggesting that the crosslink density influences the degree of segregation/domain coherence. Moreover, the curing/hot-pressing pathway governs the disruption of BCP-derived long-range ordering in these PDMS-containing vitrimerized tBCPs on the basis of the broadening of the primary peaks in SAXS analysis. The morphological characteristics of the tBCP and cured tBCP bulk films obtained via SAXS are detailed in Table 3 and shown in Fig. 7.

Guided by the SAXS measurements collected before and after vitrimer formation, we propose a nanostructure construction mechanism for tBCP networks (Scheme 2) that enables a controlled comparison of the nanoscale morphologies during curing. (A) The tBCP experiences self-assembly into microphase-separated domains before vitrimerization, resulting in a characteristic primary SAXS maximum. After curing, the tBCP samples largely follow a REMPS process, in which network formation proceeds concurrently with microphase separation, thereby locking in the preorganized nanostructure while mediating the domain contrast and structural coherence, as reflected by the systematic changes in the peak intensity and peak width. The NH_2/β-KE ratio governs the curing outcomes

as follows: (B) a near-stoichiometric NH_2/β-KE ratio promotes spatially heterogeneous crosslinking that drives local restructuring and results in less long-range order, as revealed by the occurrence of peak broadening and more diffuse scattering signatures, whereas (C) double stoichiometric ratios introduce more homogeneous network formation and better retention of the original domain periodicity (a limited peak shift with improved peak definition).

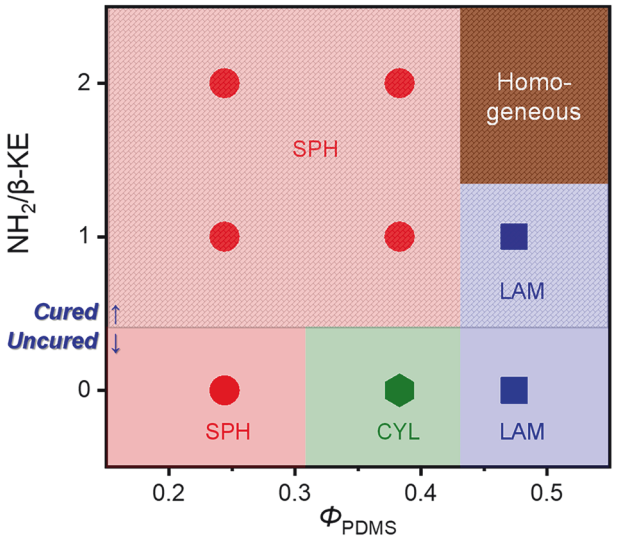

Fig. 7 Variations in microphase separation of pristine and tBCPs after vitrimerization

Conclusions

A sustainable, scalable route to PDMS-containing nanostructured vitrimers was developed by combining ppm-level SARA ATRP with vinylogous urethane network formation. Well-defined P(AAEMA-*b*-DMS-*b*-AAEMA) tBCPs were synthesized from a Br–PDMS–Br MI. With increasing Φ_{PDMS} value, canonical high-χ self-assembly in the bulk material, which transitioned from spherical to cylindrical and lamellar morphologies on a scale of ca. 30 nm, was observed. Subsequent crosslinking with HMDA and hot-pressing produced vitrimer networks with significantly increased thermal robustness ($\Delta T_{d,5\%} = +51$ °C). A comparison of SAXS measurements obtained before and after vitrimerization indicated that the practical dynamic annealing process suppresses higher-order reflections across all compositions and yields broadened primary maxima, which is consistent with a pronounced reduction in long-range lattice coherence and the emergence of largely non-ordered microphase-separated structures. Varying NH_2/β-KE from 1 to 2 modestly modulates the characteristic spacing and peak width in the profile of each composition, suggesting that the crosslinking density fine-tunes segregation and domain coherence, whereas the REMPS-driven curing process plays a dominant role in disrupting BCP-derived long-range order. In summary, these findings establish an ATRP-enabled platform for PDMS-based triblock vitrimers and clarify how network formation and stoichiometry govern nanoscale morphology retention versus transformation during vitrimerization.

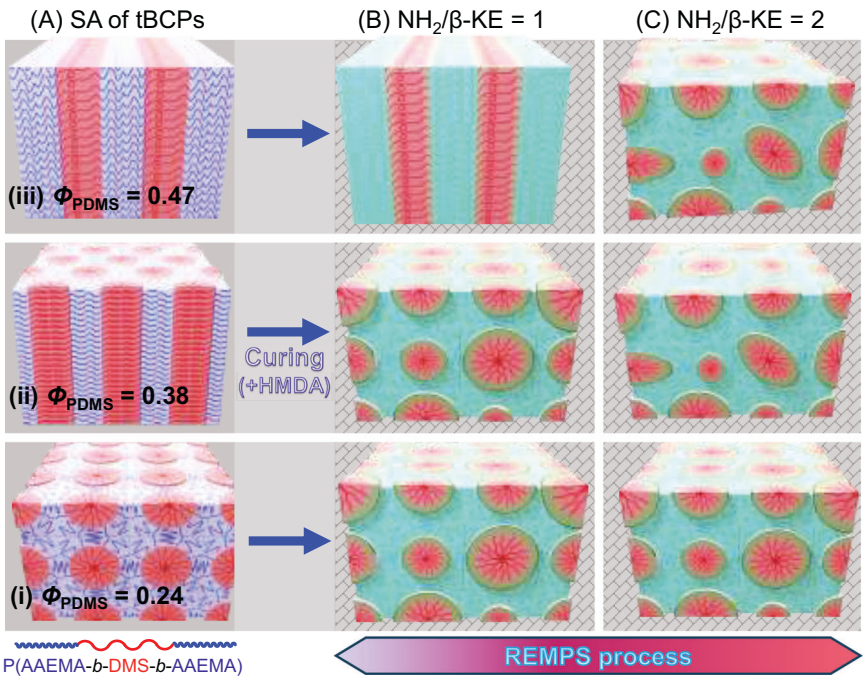

Scheme 2 Proposed microphase separation behaviors for **A** pristine tBCPs and **B, C** tBCPs after curing with various amounts of NH_2/β-KE with the REMPS process

Acknowledgements The authors thank the National Science and Technology Council for the provided financial support (NSTC114-2124-M-005-001 and NSTC113-2926-I-110-501-G).

Funding Open access funding provided by National Chung Hsing University.

Compliance with ethical standards

Conflict of interest The authors declare no competing interests.

Publisher's note Springer Nature remains neutral with regard to jurisdictional claims in published maps and institutional affiliations.

References

1. Montarnal D, Capelot M, Tournilhac F, Leibler L. Silica-like malleable materials from permanent organic networks. Science. 2011;334:965–8.
2. Denissen W, Rivero G, Nicolaÿ R, Leibler L, Winne JM, Du Prez FE. Vinylogous urethane vitrimers. Adv Funct Mater. 2015;25:2451–7.
3. Denissen W, Droesbeke M, Nicolaÿ R, Leibler L, Winne JM, Du Prez FE. Chemical control of the viscoelastic properties of vinylogous urethane vitrimers. Nat Commun. 2017;8:14857.
4. Chou LC, Mohamed MG, Kuo SW, Nakamura Y, Huang CF. Synthesis of multifunctional poly(carbamoyl ester)s containing dual-cleavable linkages and an AIE luminogen *via* Passerini-type multicomponent polymerization. Chem Commun. 2022;58:12317.
5. Nakamura Y, Huang YS, Huang CF, Samitsu S. Passerini polymerization of α-lipoic acid for dynamically crosslinking 1,2-dithiolane-functionalized polymers. Chem Commun. 2024;60:5270–3.
6. Nakamura Y, Huang YS, Huang CF. Multicomponent polymerizations of α-lipoic acid for the development of versatile adhesive materials. Eur Polym J. 2025;236:114152.
7. Hayashi M, Oba Y, Kimura T, Takasu A. Simple preparation, properties, and functions of vitrimer-like polyacrylate elastomers using trans-*N*-alkylation bond exchange. Polym J. 2021;53:835–40.
8. Suzuki Y, Shinagawa Y, Kato E, Mishima R, Fukao K, Matsumoto A. Polymerization-induced vitrification and kinetic heterogenization at the onset of the Trommsdorff effect. Macromolecules. 2021;54:3293–303.
9. Suzuki Y. Polymerization-induced vitrification, apparent phase separation, and reaction acceleration during bulk polymerization. Polym J. 2023;55:807–15.
10. Röttger M, Domenech T, van der Weegen R, Nicolaÿ R, Leibler L. High-performance vitrimers from commodity thermoplastics through dioxaborolane metathesis. Science. 2017;356:62–5.
11. Winne JM, Leibler L, Du Prez FE. Dynamic covalent chemistry in polymer networks: a mechanistic perspective. Polym Chem. 2019;10:6091–108.
12. Guerre M, Taplan C, Winne JM, Du Prez FE. Vitrimers: directing chemical reactivity to control material properties. Chem Sci. 2020;11:4855–70.
13. Bates FS, Fredrickson GH. Block copolymer thermodynamics - theory and experiment. Annu Rev Phys Chem. 1990;41:525–57.
14. Bates FS, Fredrickson GH. Block copolymers - designer soft materials. Phys Today. 1999;52:32–8.
15. Jung YS, Ross CA. Orientation-controlled self-assembled nanolithography using a polystyrene-polydimethylsiloxane block copolymer. Nano Lett. 2007;7:2046–50.
16. Boyer C, Corrigan NA, Jung K, Nguyen D, Nguyen TK, Adnan NNM, et al. Copper-mediated living radical polymerization (atom transfer radical polymerization and copper(0) mediated polymerization): from fundamentals to bioapplications. Chem Rev. 2016;116:1803–949.
17. Huang YS, Ejeta DD, Lin KY, Kuo SW, Jamnongkan T, Huang CF. Synthesis of PDMS-μ-PCL miktoarm star copolymers by combinations (Є) of styrenics-assisted atom transfer radical coupling and ring-opening polymerization and study of the self-assembled nanostructures. Nanomaterials. 2023;13:2355.
18. Huang YS, Huang CF. Synthesis of well-defined PMMA-*b*-PDMS-*b*-PMMA triblock copolymer and study of its self-assembly behaviors in epoxy resin. Eur Polym J. 2021;160:110787.
19. Huang YS, Hsueh HY, Aimi J, Chou LC, Lu YC, Kuo SW, et al. Effects of various Cu(0), Fe(0), and proanthocyanidin reducing agents on Fe(III)-catalysed ATRP for the synthesis of PMMA block copolymers and their self-assembly behaviours. Polym Chem. 2020;11:5147–55.
20. Kamigaito M. Recent developments in metal-catalyzed living radical polymerization. Polym J. 2011;43:105–20.
21. Huang CF. Surface-initiated atom transfer radical polymerization for applications in sensors, non-biofouling surfaces and adsorbents. Polym J. 2016;48:341–50.
22. Huang CF, Yokoyama A, Yokozawa T. Synthesis of polybenzamide-*b*-polystyrene block copolymer *via* combination of chain-growth condensation polymerization and atom transfer radical polymerization. J Polym Sci, Part A Polym Chem. 2010;48:2948–54.
23. Huang YS, Ejeta DD, Kuo SW, Nakamura Y, Huang CF. Combinations (Є) among controlled/living polymerizations and utilizations of efficient chemical reactions for the synthesis of novel polymeric materials. Polym Chem. 2023;14:4783–803.
24. Krys P, Matyjaszewski K. Kinetics of atom transfer radical polymerization. Eur Polym J. 2017;89:482–523.
25. Konkolewicz D, Wang Y, Zhong MJ, Krys P, Isse AA, Gennaro A, et al. Reversible-deactivation radical polymerization in the presence of metallic copper. A critical assessment of the SARA ATRP and SET-LRP mechanisms. Macromolecules. 2013;46:8749–72.
26. Konkolewicz D, Wang Y, Krys P, Zhong MJ, Isse AA, Gennaro A, et al. SARA ATRP or SET-LRP. End of controversy? Polym Chem. 2014;5:4396–417.
27. Zaborniak I, Chmielarz P. How we can improve ARGET ATRP in an aqueous system: honey as an unusual solution for polymerization of (meth)acrylates. Eur Polym J. 2023;183:111735.
28. Zaborniak I, Klamut M, Warne CM, Kisiel K, Niemiec M, Błoniarz P, et al. Controlled polymer synthesis toward green chemistry: deep insights into atom transfer radical polymerization in biobased substitutes for polar aprotic solvents. ACS Sustain Chem Eng. 2024;12:4933–45.
29. Dworakowska S, Lorandi F, Gorczyński A, Matyjaszewski K. Toward green atom transfer radical polymerization: current status and future challenges. Adv Sci. 2022;9:2106076.

30. De Bon F, B. Barbosa A, Fonseca RG, Fantin M, Serra AC, F. J Coelho J. Large volume and oxygen-tolerant photoinduced aqueous atom transfer radical polymerization. Chem Eng J. 2023;451:138777.
31. Yeow J, Chapman R, Gormley AJ, Boyer C. Up in the air: oxygen tolerance in controlled/living radical polymerisation. Chem Soc Rev. 2018;47:4357–87.
32. Huang CF, Chen WH, Aimi J, Huang YS, Venkatesan S, Chiang YW, et al. Synthesis of well-defined PCL-*b*-PnBA-*b*-PMMA ABC-type triblock copolymers: toward the construction of nanostructures in epoxy thermosets. Polym Chem. 2018;9:5644–54.
33. Michelas M, Corrigan N, Boyer C. 3D printing *via* polymerization-induced microphase separation using acrylate macromonomers instead of macroRAFT agents. Polym Chem. 2025;16:4102–12.
34. Maekawa S, Seshimo T, Dazai T, Sato K, Hatakeyama-Sato K, Nabae Y, et al. Chemically tailored block copolymers for highly reliable sub-10 nm patterns by directed self-assembly. Nat Commun. 2024;15:5671.
35. Ejeta SY, Bembalkar T, Kuo SW, Hsu MF, Wang HM, Kuo KY, et al. PCL-*b*-PnBA additives enable flexible and adhesive photoresists through microphase separation. Macromol Chem Phys. 2026;227:e00364.
36. Lee K, Corrigan N, Boyer C. Polymerization-induced microphase separation for the fabrication of nanostructured materials. Angew Chem Int Ed. 2023;62:e202307329.
37. Kalinova R, Mladenova K, Petrova S, Doumanov J, Dimitrov I. Solvent-free synthesis of multifunctional block copolymer and formation of DNA and drug nanocarriers. Nanomaterials. 2023;13:2936.
38. Lessard JJ, Scheutz GM, Sung SH, Lantz KA, Epps T, Sumerlin BS. Block copolymer vitrimers. J Am Chem Soc. 2020;142:283–9.
39. Asempour F, Laurent E, Bride T, Maric M. Rheological and mechanical comparison of di-and tri-block copolymer imine vitrimers. Eur Polym J. 2024;219:113402.
40. Fang HG, Gao XC, Zhang F, Zhou WJ, Qi GB, Song K, et al. Triblock elastomeric vitrimers: preparation, morphology, rheology, and applications. Macromolecules. 2022;55:10900–11.
41. Lai KY, Huang YS, Chu CY, Huang CF. Synthesis of poly(*N*-H benzamide)-*b*-poly(lauryl methacrylate)-*b*-poly(*N*-H benzamide) symmetrical triblock copolymers by combinations of CGCP, SARA ATRP, and SA ATRC. Polymer. 2018;137:385–94.

Affiliations

Yi-Shen Huang[1,2] · Shibiru Yadeta Ejeta[1,3] · Shiao-Wei Kuo[4] · Yeo-Wan Chiang[4] · Yasuyuki Nakamura[2] · Chih-Feng Huang[1,5]

[1] Department of Chemical Engineering, i-Center for Advanced Science and Technology (iCAST), National Chung Hsing University, Taichung, Taiwan, ROC

[2] Research Center for Macromolecules and Biomaterials, National Institute for Materials Science, Tsukuba, Japan

[3] Department of Chemistry, College of Natural and Computational Sciences, Wallaga University, Nekemte, Ethiopia

[4] Department of Materials and Optoelectronic Science, Center for Functional Polymers and Supramolecular Materials, National Sun Yat-Sen University, Kaohsiung, Taiwan, ROC

[5] Graduate Program in Semiconductor and Green Technology, Academy of Circular Economy, National Chung Hsing University, Nantou City, Taiwan, ROC